LANGMUIR

pubs.acs.org/Langmuir Article

Digital Microfluidics: Magnetic Transportation and Coalescence of Sessile Droplets on Hydrophobic Surfaces

Md Rifat Hassan, Jie Zhang, and Cheng Wang*

Cite This: *Langmuir* 2021, 37, 5823−5837 Read Online

ACCESS | Metrics & More | Article Recommendations | Supporting Information

ABSTRACT: Magnetic digital microfluidics is advantageous over other existing droplet manipulation methods, which exploits magnetic forces for actuation and offers the flexibility of implementation in resource-limited point-of-care applications. This article discusses the dynamic behavior of a pair of sessile droplets on a hydrophobic surface under the presence of a permanent magnetic field. A phase field method-based solver is employed in a two-dimensional computational domain to numerically capture the dynamic evolution of the droplet interfaces, which again simultaneously solves the magnetic and flow fields. On a superhydrophobic surface (i.e., $\theta_c = 150°$), the nonuniform magnetic field forces the pair of sessile droplets to move toward each other, which eventually leads to a jumping off phenomenon of the merged droplet from the solid surface after coalescence. Also, there exists a critical magnetic Bond number Bo_m^{cr}, beyond which no coalescence event between droplets is observed. Moreover, on a less hydrophobic surface ($\theta_c \leq 120°$), the droplets still coalesce under a magnetic field, although the merged droplet does not experience any upward flight after coalescence. Also, the merging phenomenon at lower contact angle values (i.e., $\theta_c = 90°$) appears significantly different than at higher contact angle values (i.e., $\theta_c = 120°$). Additionally, if the pair of sessile droplets is dispersed to a different surrounding medium, the viscosity ratio plays a significant role in the upward flight of the merged droplet, where the coalesced droplet exhibits increased vertical migration at higher viscosity ratios.

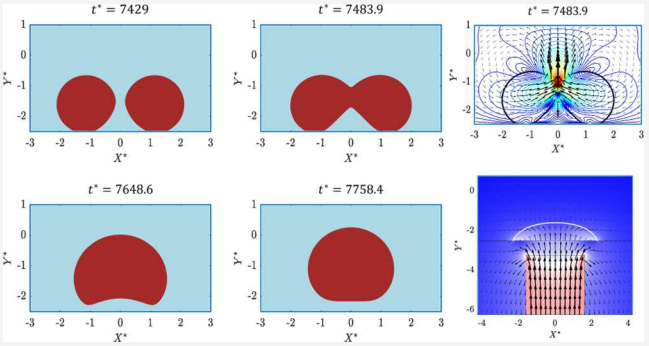

INTRODUCTION

Digital microfluidics deals with the behavior of sessile droplets on an open surface and in combination with emulsion microfluidics are crucial building blocks of droplet-based microfluidics, which has been prevalent as a well-established research field in the literature for over a decade now. One of the main advantages of digital microfluidics over emulsion microfluidics (also known as continuous flow droplet-based microfluidics) is that emulsion microfluidics requires an external pumping mechanism to attain continuous generation of droplets through a closed microfluidic channel, whereas in digital microfluidics, manipulation of droplets takes place on an open plain surface without any confinement, which in turn enables droplets to act as independent virtual reactors that are often utilized in point-of-care diagnostics, which requires synthesis of hazardous materials[1,2] or preparation of complex samples[3−6] and cell-based assays.[7]

In general, the dynamic motion of a sessile droplet on a substrate can be exploited using gravity, given the fact that the droplet volume is large enough, which further can be magnified through an increase in the tilting angle or the hydrophobicity of the substrate, whereas surface tension plays a crucial role in the dynamics of smaller volume droplets. However, because gravitational and surface tension forces pose significant limitations, droplets in digital microfluidics can be actuated through other mechanisms, such as, electrowetting on dielectric (EWOD),[8−10] magnetic,[11−14] and surface acoustic waves.[15,16] Among the abovementioned mechanisms, EWOD is the most popular one, which is capable of splitting and dispensing droplets, but requires electrodes to work that in turn provides little flexibility in operations. In contrast, magnetic actuation does not require any external sources and offers manual control, which is critical in resource-limited environmental applications, where availability of electricity is not always guaranteed. Another great advantage of magnetic actuation is its higher tolerance to liquid properties, while electrowetting actuation is massively dependent on the permittivity, conductivity, and surface tension of the liquid, which requires higher driving voltage in manipulation operations.[7] An in-detailed description on the

Received: January 15, 2021
Revised: March 9, 2021
Published: May 7, 2021

https://doi.org/10.1021/acs.langmuir.1c00141
Langmuir 2021, 37, 5823−5837

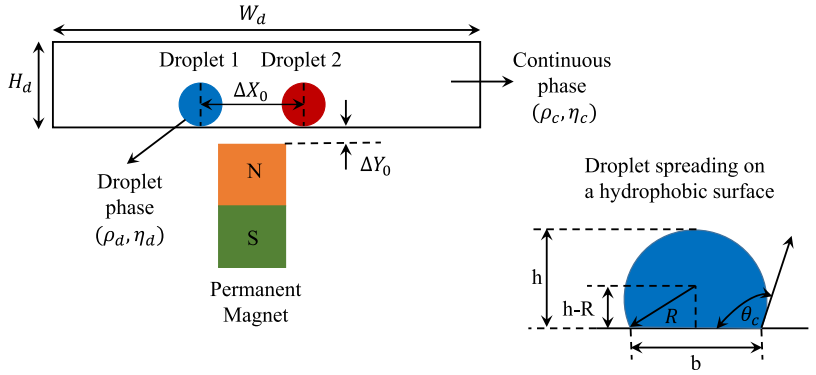

Figure 1. Graphical representation of a pair of sessile ferrofluid droplets dispersed in an immiscible and viscous continuous fluid phase under a permanent magnetic field, $\mathbf{H}_0$.

advantages of magnetic actuation over EWOD actuation is provided by Zhang and Nguyen.[17]

Dual functionality of magnetic particles is one of the most striking features in magnetic actuation-based digital microfluidics, where the magnetic particles, in addition to droplet actuation, function as a solid substrate for molecule adsorption. Pipper et al.[5] found out that under the exposure to magnetic forces, droplets containing silica-functionalized superparamagnetic particles are capable of identifying pathogenic avian influenza virus (H5N1) on a throat swab sample. Moreover, Long et al.[18] investigated the particle extraction behavior of droplets and realized that the magnetic particles' mass and movement speed of a permanent magnet play a decisive role in the manipulation of droplets, leading to breakup under certain operating conditions, while the effects of different hydrophobic surfaces on the magnetic actuated motion of droplets are analyzed by Mats et al.[19] Kim et al.[20] proposed a magnetic bead droplet immunoassay microfluidic platform that is extremely sensitive to the detection of oligomer Aβ for Alzheimer's disease and simultaneously simplifies the enzyme-linked immunosorbent assay (ELISA) process. Similar investigations on the ELISA process are also performed by several other authors, where the magnetic particles are treated with antibodies to capture the target molecules.[21,22]

Droplet manipulation in microfluidics applications is usually accomplished either by controlling the behavior of magnetic particles by a permanent magnet or an array of electromagnets that consists of microcoils. Okochi et al.[23] controlled droplets with magnetic particles by placing a permanent magnet below the channel surface and achieved coalescence with a lysis buffer droplet, while a simple configuration of the total RNA extraction droplet array is presented by Shi et al.,[24] which facilitates the transportation of magnetic beads through buffer solutions. In contrast, several other analytical and numerical studies[14,25−28] implemented microcoils as electromagnets in order to achieve controlled transportation of magnetic droplets; however, one of the major issues arises as a result of using electromagnets, which is known as Joule heating and in turn requires a cooling mechanism to mitigate the heating effect.[11]

Ferrofluids are another examples of a liquid magnet, which contain colloidal suspensions of magnetic nanoparticles in a carrier fluid and experience deformation under the exposure to magnetic fields.[29−34] Also, due to the uniform distribution of magnetic nanoparticles, ferrofluids can be transported to different locations for liquid phase reactions[35] and are conventionally used as a sealant[36] in hard drives and a coolant in loudspeakers.[37] Nguyen et al.[38] conducted experiments on the motion of a droplet under a moving permanent magnetic field and derived a critical velocity, above which the droplet fails to move with the same velocity as the moving magnet. Moreover, Beyzavi and Nguyen demonstrated one-dimensional[26] and two-dimensional (2D)[39] manipulation of the ferrofluid droplet using micro coil arrays and found that a small magnetic field gradient is enough to induce movement in a ferrofluid droplet, while Egatz-Gómez et al.[40] observed coalescence between two water drops under a moving permanent magnetic field.

Droplet coalescence is an event where two or more droplets, following large deformations and rupture of the interface separating the droplets, merge into one single droplet upon contact. Moreover, this coalescence process is critical to the understanding of a range of science and engineering applications, including raindrop formation in clouds,[41,42] sintering in metallurgy,[43] and spray painting/coating.[44,45] In these applications, the coalescence rate of adjacent drops plays a vital role in the determination of the material properties of the solidified precursor. More importantly, coalescence of drops is an integral step in controllable droplet-based functions in microfluidics, such as micromixing[10,46] and microreaction[47,48] in lab-on-a-chip devices, where advective mixing during coalescence is used to control chemical and biological assays. Several numerical studies on the coalescence of sessile droplets have also been reported in the literature.[49−51] Shi et al.[52] implemented a lattice Boltzmann method to analyze the coalescence pattern of droplets on a textured surface and found that surface roughness affects the jumping phenomenon of the merged droplet. Liu et al.[53] performed an investigation on the coalescence-induced self-propelled jumping behavior of droplets on a patterned hydrophobic surface, while a similar analysis is conducted by Wang et al.[54] Recently, Liu and Liu[55] have succeeded in transporting a sessile droplet to different locations along a hydrophobic surface through the application of an electric field. However, the current numerical studies in the literature only focused on larger-sized droplets,[49,50] so that gravitational forces can induce coalescence between droplets that are initially placed in contact with each other or droplets on patterned surfaces.[52,53] Moreover, as per our knowledge, till now, no one has ever performed numerical analyses on the dynamic behavior of micrometer-sized droplets (where gravitational forces are negligible in compared to viscous forces) on an open surface under the presence of magnetic fields that will be useful to a wide range of microfluidics applications, including biological and chemical assays.[35,38,56−62] As a result, in this article, we numerically investigate the dynamics of a pair of sessile droplets on a hydrophobic surface under the effect of a permanent

https://doi.org/10.1021/acs.langmuir.1c00141
Langmuir 2021, 37, 5823−5837

magnetic field, which ultimately leads to a coalescence-induced jumping/no jumping phenomenon under certain operating conditions. Here, a 2D computational scheme is adopted, which is widely proven to capture the dynamic evolution of the droplet interface with great precision, while minimizing the use of a considerable amount of computational resources,[29−33] which further facilitates in the investigation on the effects of a wide range of parameters, that is, magnetic field strength, contact angle, and viscosity ratio on the dynamics of droplets on hydrophobic surfaces.

The paper is organized as follows: in the Numerical Model section, we depict the numerical setup of the computational model, while an in-detailed description of the computational algorithm and governing equations are provided in the Numerical Method section. Next, the effects of different parameters, that is, magnetic field strength, contact angle, and viscosity ratio on the dynamic behavior of a pair of sessile droplets are explained in Results and Discussions, which is subsequently followed by the validation of the numerical model and behavior of droplets under a solitary magnetic field. Finally, the critical findings are summarized in the Conclusion section. Additionally, the efficacy of the phase-field (PF) method in conserving the mass of the droplet and grid independence check is provided in the Supporting Information.

NUMERICAL MODEL

Figure 1 depicts the graphical representation of a pair of sessile ferrofluid droplets dispersed in another fluid medium under a permanent magnetic field, $\mathbf{H}_0$. In this investigation, both fluid phases (i.e., continuous and droplet phases) are treated as immiscible, viscous, and Newtonian fluids. In the beginning, the droplet phase is considered equally dense and viscous as the continuous phase (i.e., $\rho_d = \rho_c$ and $\eta_d = \eta_c$), where the subscripts d and c denote the droplet and continuous phases, respectively. Also, the droplet contains magnetic properties and has a magnetic permeability equal to $5\mu_0$ (i.e., $\mu_d = 5\mu_0$), while the surrounding medium is treated as a nonmagnetic fluid (i.e., $\mu_c = \mu_0$). The height of the computational domain is considered five times the initial radius of the droplet R_0 (i.e., $H_d = 5R_0$), while the width equals to $5H_d$ (i.e., $W_d = 5H_d$) to ignore the effect of the side walls on the dynamic behavior of the droplets.

Initially, a pair of identical ferrofluid droplets with initial radii R_0 are separated by a distance ΔX_0 in the horizontal direction, while maintaining an initial contact with the solid surface at the bottom interface of the droplet. Next, a permanent magnetic field, $\mathbf{H}_0$, is applied at the bottom of the droplet domain, which maintains a vertical separation distance ΔY_0 between the top surface of the magnet and bottom wall of the droplet domain. Also, the distance between the center of the magnet and the centroids of droplets along the horizontal direction are set equal to each other. Under the combined effects of the wetted wall condition and magnetic field, the wettability of the droplets changes, and the wettability of the droplets can be characterized by the spreading diameter b and apex height h, respectively. Additionally, as the wettability of the droplets changes, the contact angle θ_c of the droplets undergoes a transition, which can be defined as the angle the droplet interface makes with the outline of the contact surface (horizontal solid surface) and is useful in determining the surface free energy of a solid material. In order to perform numerical simulations, the bottom wall of the computational domain is subjected to a wetted wall condition, while a pressure outlet boundary condition is employed to the top wall to ensure that the droplets are free from any pressure and velocity gradient effects. The PF method uses a condition called "wetted wall", which defines the contact angle between the droplets and bottom substrate in two-phase flows.[63] Additionally, a periodic boundary condition is applied to the side walls to ensure infinite periodicity in the x direction. Next, a magnetization constitutive relation is applied to the permanent magnet to generate the magnetic fields. Finally, a finite element method-based commercial numerical solver (COMSOL 5.3) is implemented to capture the dynamic behavior of droplet interfaces under permanent magnetic fields, which couples both flow and magnetic fields. For the convenience of the readers, the simulation parameters and the corresponding magnitudes are listed in Table 1.

Table 1. Simulation Parameters and Magnitudes

parameter	symbol	value	unit
channel width	W_d	500	μm
channel height	H_d	100	μm
permeability of vacuum	μ_0	$4\pi \times 10^{-7}$	H/m
initial droplet radius	R_0	20	μm
interfacial tension	σ	0.0135	N/m
density of the droplet phase	ρ_d	1260	kg/m^3
viscosity of the droplet phase	η_d	0.105	Pa·s
horizontal separation distance	ΔX_0	60	μm
vertical separation distance	ΔY_0	15	μm
magnetic permeability of the droplet phase	μ_d	$5\mu_0$	H/m
magnetic permeability of the continuous phase	μ_c	μ_0	H/m

NUMERICAL METHOD

PF Method. Multiphase flows, in general, can occur in various forms, such as transition of the liquid phase into the vapor phase due to external heating and dispersed flows, where one phase exists in the form of particles, droplets, or bubbles in a continuous phase, that is, liquid or gas. However, one of the most common difficulties that arises in solving multiphase flow problems involving droplets is to track the free interface of the droplet that experiences severe deformation over time under external forces and flow conditions. As a result, a PF method, governed by a Cahn−Hilliard equation, is implemented in our model to track the diffuse interface of the droplet separating the immiscible fluid phases, which also provides a greater advantage over the level set (LS) method in terms of conserving the mass of droplets. Note that the numerical methods involving diffuse interfaces are usually constructed with an idea that they are not sharp boundaries, rather have finite width, and are distinguished by smooth and rapid transitions in different physical quantities, that is, density, viscosity, and so forth.

The PF method involves a dimensionless variable ϕ that differentiates different phases, which has a constant value −1 in the bulk phase (i.e., $\phi_c = -1$) and 1 in the dispersed droplet phase (i.e., $\phi_d = 1$), followed by a smooth transition between −1 and 1 (i.e., $-1 < \phi < 1$) in a hyperbolic tangent or similar manners. When $\phi = 0$, it defines the exact interface of the droplet. Because the Cahn−Hilliard equation involves fourth-order derivative, our finite element method-based numerical solver splits the equation into two second-order equations

https://doi.org/10.1021/acs.langmuir.1c00141
Langmuir 2021, 37, 5823−5837

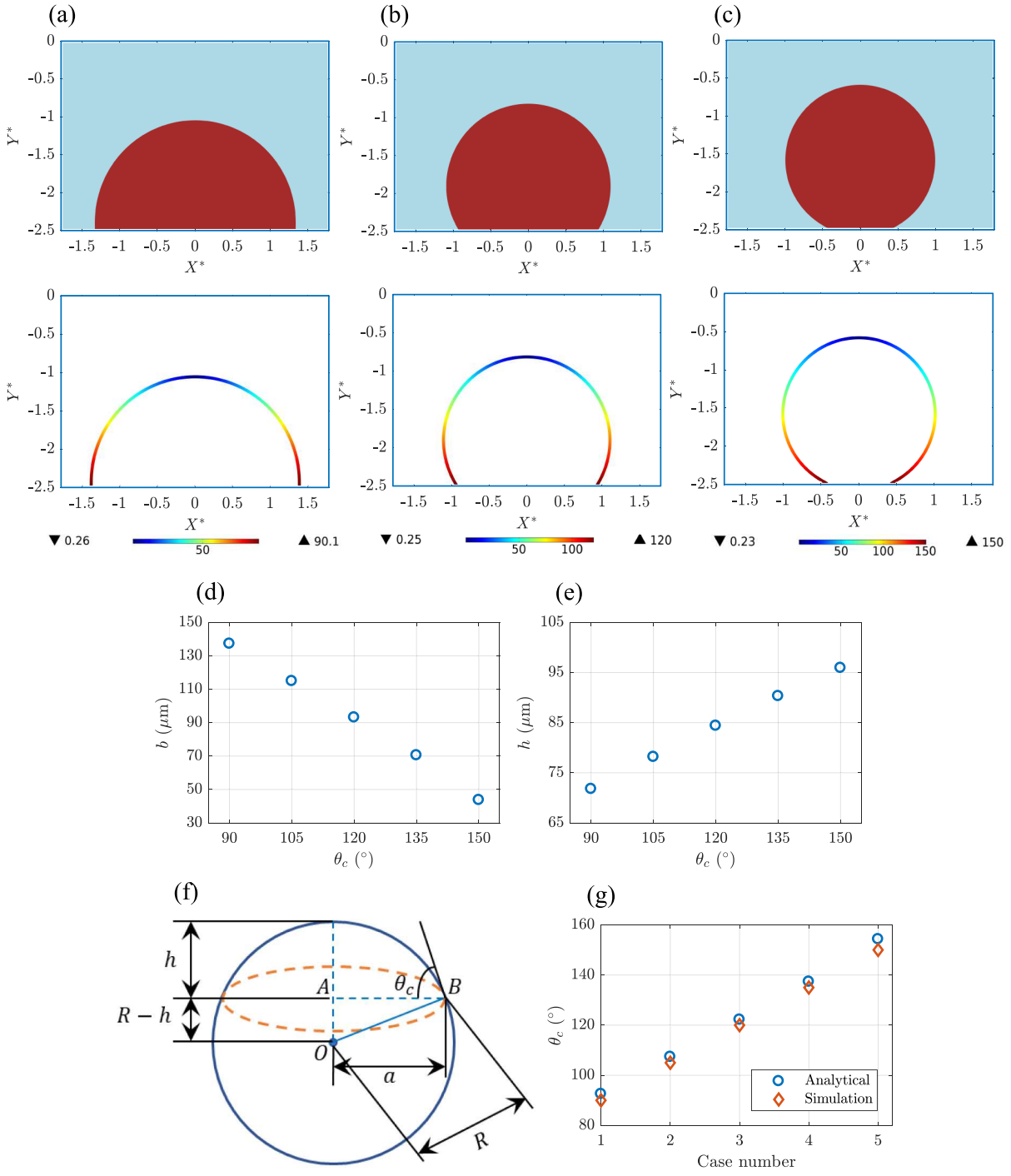

Figure 2. Equilibrium droplet shapes with the contact angle on a solid horizontal surface. (a) $\theta_c = 90°$; (b) $\theta_c = 120°$; (c) $\theta_c = 150°$; (d) base diameter b vs contact angle θ_c; (e) height h vs contact angle θ_c; (f) schematic for derivation of the contact angle relationship in terms of base diameter and height of a droplet; and (g) comparison of simulated contact angle θ_c results against analytical relationships.

$$\frac{\partial \phi}{\partial t} + \mathbf{u}\cdot\nabla\phi = \nabla\gamma\nabla G$$

$$G = \lambda\left[-\nabla^2\phi + \frac{\phi(\phi^2 - 1)}{\epsilon^2}\right] \quad (1)$$

where $\mathbf{u}$ and G denote the flow velocity in the domain (m/s) and chemical potential of the system, respectively. The parameter γ represents the mobility (m^3·s/kg), which also determines the time scale of diffusion and is related to the thickness of the droplet interface ϵ (m) through the following equation

$$\gamma = \chi\epsilon^2 \quad (2)$$

where χ is the mobility tuning parameter (m·s/kg). The mobility parameter γ needs a careful handling in the numerical approach, so that it is large enough to retain a constant interfacial thickness but small enough to avoid the overdamping of the convective terms. Moreover, the relationship among the mixing energy density λ, interface thickness ϵ, and surface tension coefficient σ can be expressed through the following equation

https://doi.org/10.1021/acs.langmuir.1c00141
Langmuir 2021, 37, 5823−5837

$$\sigma = \frac{2\sqrt{2}}{3}\frac{\lambda}{\epsilon} \tag{3}$$

In our model, the interface thickness ϵ is considered half the maximum mesh size h_m in the region passed by the droplet interface during its movement along the domain (i.e., $\epsilon = h_m/2$). In the PF method, the volume fractions of different fluid phases are described as

$$V_{f1} = \frac{1-\phi}{2},\ V_{f2} = \frac{1+\phi}{2} \tag{4}$$

Moreover, because the PF method considers a multiphase flow as a single phase flow, the different properties in the flow domain such as density (ρ) and viscosity (η) can be calculated using volume fractions of fluid phases as

$$\rho = \rho_c + (\rho_d - \rho_c)V_{f2},\ \eta = \eta_c + (\eta_d - \eta_c)V_{f2} \tag{5}$$

Governing Equations. The flow dynamics of an isothermal and incompressible system involving two different Newtonian fluid phases is governed by the incompressible Navier−Stokes equations

$$\nabla\cdot\mathbf{u} = 0 \tag{6}$$

and

$$\rho\frac{\partial \mathbf{u}}{\partial t} + \rho(\mathbf{u}\cdot\nabla)\mathbf{u} = -\nabla p + \nabla\cdot\eta[(\nabla\mathbf{u}) + (\nabla\mathbf{u})^T] + \mathbf{F}_g + \mathbf{F}_\sigma + \mathbf{F}_m \tag{7}$$

In the abovementioned equations, p denotes the terms related to pressure, while the viscous stress tensor terms are denoted by $\eta[(\nabla\mathbf{u}) + (\nabla\mathbf{u})^T]$. On the other hand, the gravitational forces are represented by $\mathbf{F}_g$, which again equals to $\rho\mathbf{g}$, and the magnetic and surface tension forces are portrayed by the symbols $\mathbf{F}_m$ and $\mathbf{F}_\sigma$, respectively. The surface tension force $\mathbf{F}_\sigma$ can be calculated using the chemical potential of the system G (mentioned in eq 1) and PF variable ϕ as

$$\mathbf{F}_\sigma = G\nabla\phi \tag{8}$$

Due to the application of the magnetic field, the droplet interface experiences additional magnetic stresses, which can be expressed as τ_m and are required to evaluate magnetic forces $\mathbf{F}_m$. The quantification of the magnetic force $\mathbf{F}_m$ is as follows[64]

$$\mathbf{F}_m = \nabla\cdot\tau_m = \nabla\cdot\left(\mu\mathbf{H}\mathbf{H} - \frac{\mu}{2}H^2\mathbf{I}\right) \tag{9}$$

In eq 9, μ represents the permeability of the flow domain, which can be evaluated using PF variable ϕ, and $H^2 = |\mathbf{H}|^2$, whereas $\mathbf{I}$ denotes the identity operator. Additionally, the calculation of magnetic stresses requires an inclusive understanding of Maxwell equations and the constitutive relationships among magnetization $\mathbf{M}$, magnetic field $\mathbf{H}$, and magnetic induction $\mathbf{B}$, which are elucidated as follows

$$\mathbf{M} = \chi\mathbf{H},\ \nabla\times\mathbf{H} = 0,\ \nabla\cdot\mathbf{B} = 0,\ \text{and}\ \mathbf{B} = \mu_0(\mathbf{H}+\mathbf{M}) = \mu_0(1+\chi)\mathbf{H} \tag{10}$$

where μ_0 denotes the permeability of vacuum, which again equals to 1.257×10^{-6} H/m. A magnetic scalar potential ψ is defined, so that $\mathbf{H} = -\nabla\psi$, which eventually leads to the following relationship

$$\nabla\cdot(\mu\nabla\psi) = 0 \tag{11}$$

In our numerical simulation, the magnetic field $\mathbf{H}$ is solved using eq 11, which then contributes to the quantification of the magnetic forces in eq 9.

RESULTS AND DISCUSSION

Droplet Dynamics on a Solid Surface. The flow dynamics of sessile droplets is dependent on the deformation experienced by the droplets, which is predominantly influenced by the competition among viscous forces, surface tension forces, magnetic forces, and surface adhesion forces. Here, in this section, at first, we analyze the dynamic behavior of a solitary sessile droplet on a horizontal smooth surface under different wetting wall conditions. Note that the dimensions in the x and y axes are nondimensionalized by the initial radius of the droplet R_0, while density ρ, initial radius of the droplet R_0, and surface tension coefficient σ are used as scaling parameters for dimensionless time, which are as follows

$$X^* = \frac{x}{R_0},\ Y^* = \frac{y}{R_0},\ \text{and}\ t^* = t\sqrt{\frac{\sigma}{\rho {R_0}^3}} \tag{12}$$

Figure 2 depicts the equilibrium droplet shapes with the contact angle on a solid horizontal surface, and from Figure 2a−c, the equilibrium droplet shapes suggest that as the contact angle between the droplet interface and bottom wall increases (i.e., more hydrophobic), the wettability of the droplet decreases. Consequently, the base diameter of the droplet b decreases, which in turn gives rise to the magnitude of apex height h in order to conserve the total volume of the droplet. Moreover, the contact angle in each case is found to be in good agreement with the set wetted wall conditions, which again proves the accuracy of the model. Furthermore, the magnitudes of the base diameter b and height h of the droplet under different wetted wall conditions are illustrated in Figure 2d,e, which shows a decreasing and increasing trend in magnitudes with the increases in contact angle values, respectively.

In the absence of gravitational forces, a sessile droplet will form a perfect spherical cap on the bottom substrate. Figure 2f represents the schematic for derivation of the contact angle relationship in terms of base diameter b and height of the droplet h, where R is the radius of the sphere and θ_c is the contact angle. Now, applying the Pythagorean theorem in ΔOAB, we have

$$R^2 = (R-h)^2 + a^2 \tag{13}$$

Because, in our case, $a = b/2$, eq 13 becomes

$$R^2 = (R-h)^2 + \left(\frac{b}{2}\right)^2 \tag{14}$$

Simplifying eq 14, the radius of the sphere R can be expressed in terms of b and h

$$R = \frac{4h^2 + b^2}{8h} \tag{15}$$

Subsequently, the radius of the droplet R is utilized in finding the contact angle θ_c, which can be approximated as follows

$$\theta_c = \tan^{-1}\frac{b}{2(R-h)} \tag{16}$$

Using the abovementioned geometrical relationships (eqs 15 and 16), the contact angles are calculated and compared against simulated contact angles (Figure 2g), which appear to agree quantitatively very well with each other. Even, for the maximum

https://doi.org/10.1021/acs.langmuir.1c00141
Langmuir 2021, 37, 5823−5837

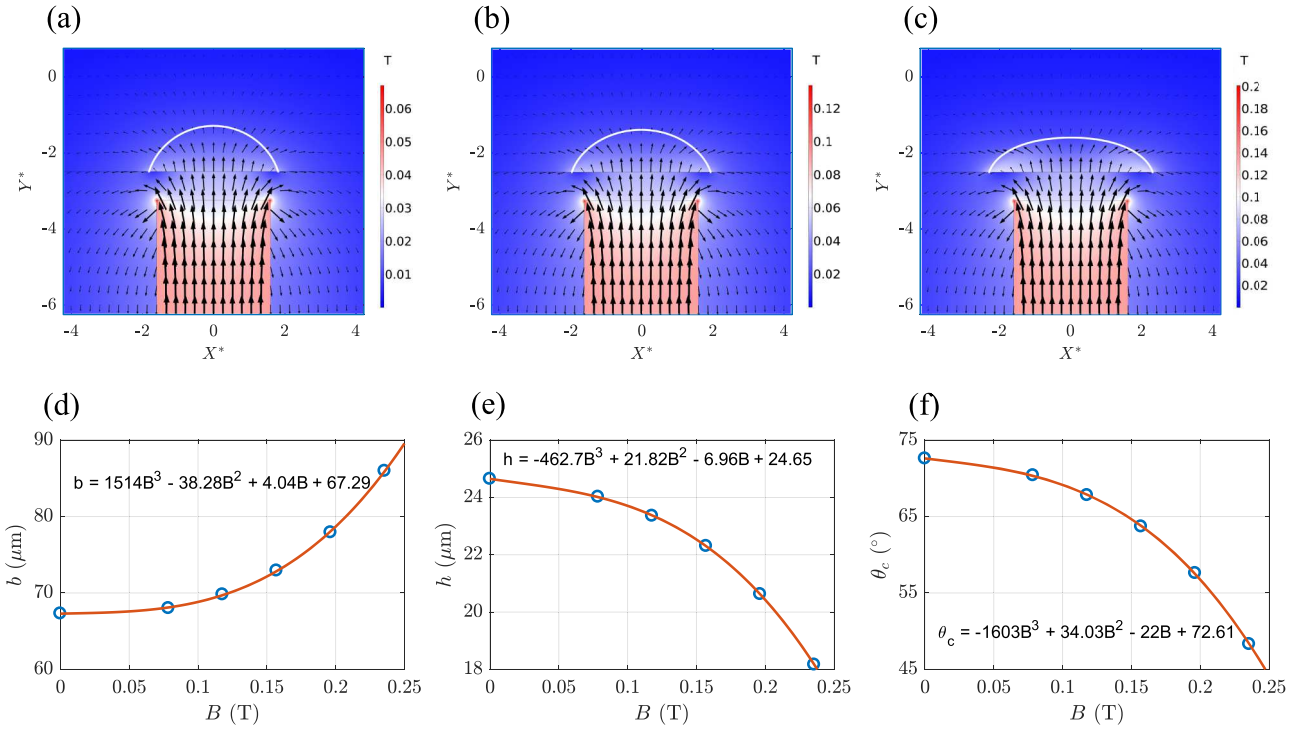

Figure 3. Steady-state shapes of the droplet on a hydrophilic smooth solid surface under a permanent magnetic field with an initial contact angle θ_c^0 = 72°. (a) **B** = 0.078 T; (b) **B** = 0.157 T; and (c) **B** = 0.2 T. (d−f) Variation in spreading characteristics of a droplet on a homogeneous solid surface under a permanent magnet along the central portion of the droplet. (d) Base diameter b; (e) height h; and (f) contact angle θ_c.

contact angle value used in the analysis (θ_c = 150°), the numerical error between the analytical and simulated contact angle is found to be approximately 2.79%.

Sessile Droplet under the Nonuniform Magnetic Field. Now, we investigate the effect of a permanent magnetic field on the wetting phenomenon of a sessile ferrofluid droplet (also known as magnetowetting), and the steady-state shapes of a sessile ferrofluid droplet under a nonuniform magnetic field are illustrated in Figure 3a−c. In the absence of a magnetic field, the droplet assumes a contact angle of 72° with the solid surface; however, as the magnetic field is applied, the shape of the droplet changes, which eventually changes the spreading dynamics of a ferrofluid droplet under magnetic fields. Figure 3a−c demonstrates that a stronger magnetic field pulls down and laterally stretches the droplet, causing an increase in the base diameter of the droplet, which in turn augments the wettability of a sessile ferrofluid droplet. Consequently, the droplet experiences a decline in its apex height and contact angle with the increase in wettability of the droplet. Moreover, the magnetic field profiles in Figure 3a−c suggest that the magnetic field lines exit the north pole of the magnet and enters the south pole through an elliptic fashion, while being parallel to each other and maintaining a symmetric profile with respect to the y axis of the computational domain. Also, the magnetic field is strongest near the vicinity of the magnet, which is eventually encountered by the ferrofluid droplet and diminishes to zero far away from the magnet.

Furthermore, the spreading characteristics of a sessile ferrofluid droplet under a nonuniform magnetic field are shown in Figure 3d−f, which indicate an increase in base diameter b (Figure 3d) and decrease in height h (Figure 3e) and contact angle θ_c (Figure 3f) magnitudes of the droplet with the increase in magnetic field strengths, and these results agree qualitatively well with the experimental findings of Nguyen et al.[38] Additionally, the spreading characteristics of the ferrofluid droplet in Figure 3d−f are found to match perfectly with a third-order polynomial fitting curve under the presence of a nonuniform magnetic field.

Magnetic Field-Induced Coalescence of Sessile Droplets. The results from previous sections indicate that the spreading characteristics of a solitary sessile ferrofluid droplet can be modified using different magnetic field strengths and wetted wall conditions. Now, in this section, we analyze the pairwise interaction between a pair of sessile ferrofluid droplets on a hydrophobic surface under the action of a permanent magnetic field. Here, some dimensionless groups (i.e., ζ and λ) are introduced, which signify the density and viscosity ratios, respectively, and are defined as

$$\zeta = \frac{\rho_d}{\rho_c}, \quad \lambda = \frac{\eta_d}{\eta_c} \tag{17}$$

whereas the magnetic Bond number Bo_m relates the magnetic and surface tension forces through the following relationship

$$Bo_m = \frac{\mu_0 R_0 H_0^{\,2}}{2\sigma} \tag{18}$$

Figure 4a illustrates the effect of the nonuniform magnetic field on the interaction phenomenon between a pair of sessile droplets on a hydrophobic surface (θ_c = 150°) at Bo_m = 0.145, ζ = 1, and λ = 1, and it can be seen that with the evolution of time (t^* = 5489.4, 7429), as the magnetic field activates, the droplets start to approach each other along the direction of the magnet. During this sliding motion, the interface of the droplets closer to the permanent magnet experiences larger deformation due to greater magnitudes of the magnetic force and tends to drag the droplet toward the magnet, while the droplet interfaces on the opposite side, being approximately circular in shape, strive to resist the movement and keep the droplet attached to the

https://doi.org/10.1021/acs.langmuir.1c00141
Langmuir 2021, 37, 5823−5837

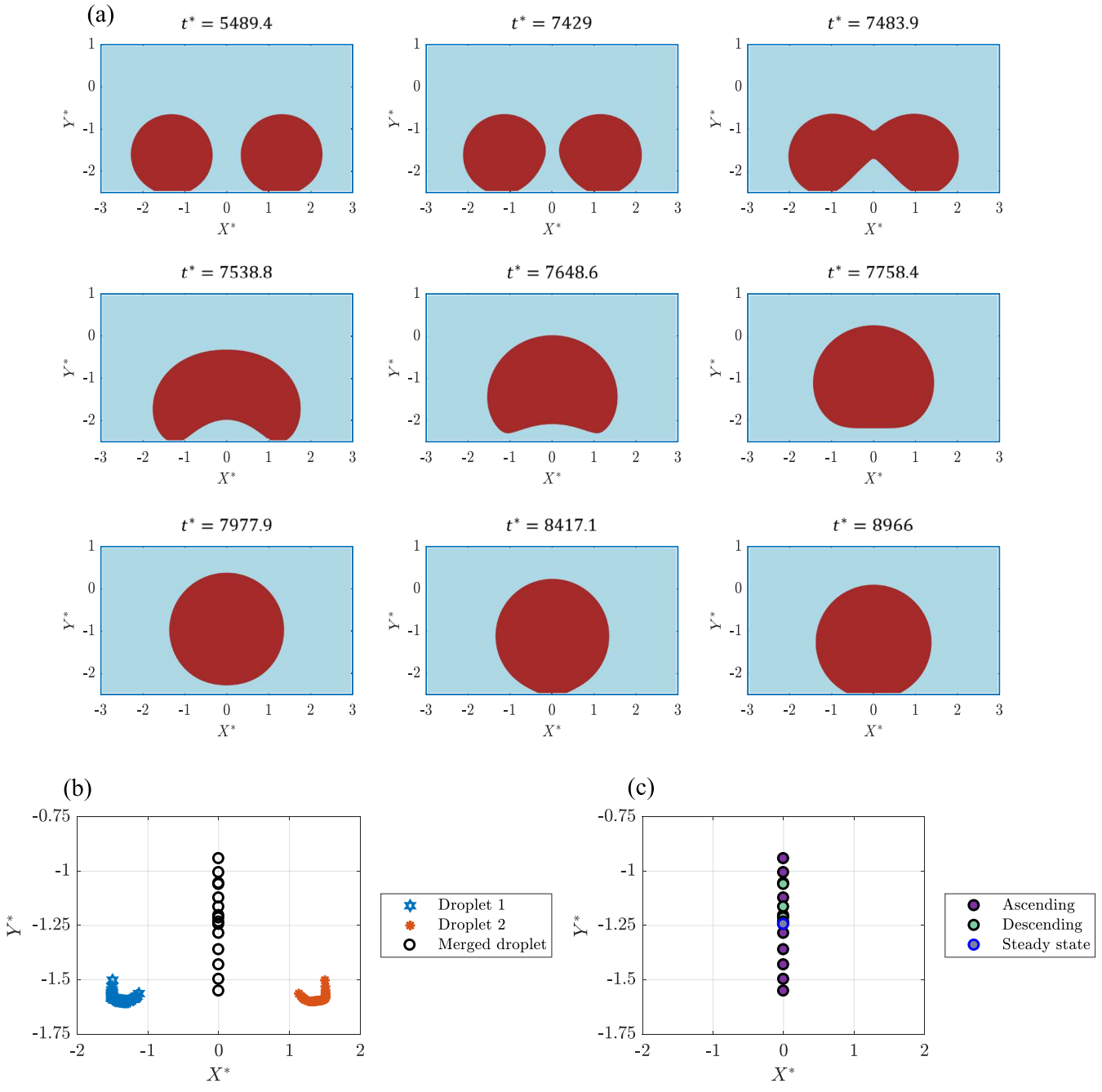

Figure 4. (a) Time evolution of the sessile droplet movement leading to coalescence and jumping off the hydrophobic surface under the permanent magnetic field at $Bo_m = 0.145$, $\theta_c = 150°$, $\zeta = 1$, and $\lambda = 1$. (b,c) Trajectory of sessile droplets on a hydrophobic surface under the permanent magnetic field at $Bo_m = 0.145$, $\theta_c = 150°$, $\zeta = 1$, and $\lambda = 1$. (b) Overall trajectory and (c) trajectory of the merged droplet.

bottom surface of the domain. As a result, during the motion, a difference between the advancing contact angle θ_a and receding contact angle θ_r emerges, which ultimately gives rise to the capillary force that eventually provides resistance to the droplet movement along the direction of the magnet. Moreover, the capillary force $\mathbf{F}_c$ is dependent on the base diameter b and surface tension coefficient σ, which can be expressed as

$$\mathbf{F}_c = b\sigma(\cos\theta_r - \cos\theta_a) \tag{19}$$

Subsequently, the magnetic field brings the droplets in close proximity with each other, where the drainage of the fluid film between the droplets occurs, which is ultimately followed by the flattening of the interfaces in the merging region ($t^* = 7483.9$). Eventually, the van der Waals intermolecular forces come into play and dominate the coalescence phenomenon between the droplets, and this event is similar to the coalescence phenomenon observed between droplet pairs in shear flows in our previous work.[32,34] Also, the force balance along the x axis during the sliding motion leading to coalescence can be demonstrated in the following form

$$\mathbf{F}_m = \mathbf{F}_c + \mathbf{F}_{ad} \tag{20}$$

where $\mathbf{F}_{ad}$ represents the adhesion forces during the motion and is proportional to the base diameter of the droplet (i.e., $\mathbf{F}_{ad} \propto b$). Note that the capillary force appears in a droplet due to cohesive forces, where the molecules of the droplet attract each other. In

https://doi.org/10.1021/acs.langmuir.1c00141
Langmuir 2021, 37, 5823−5837

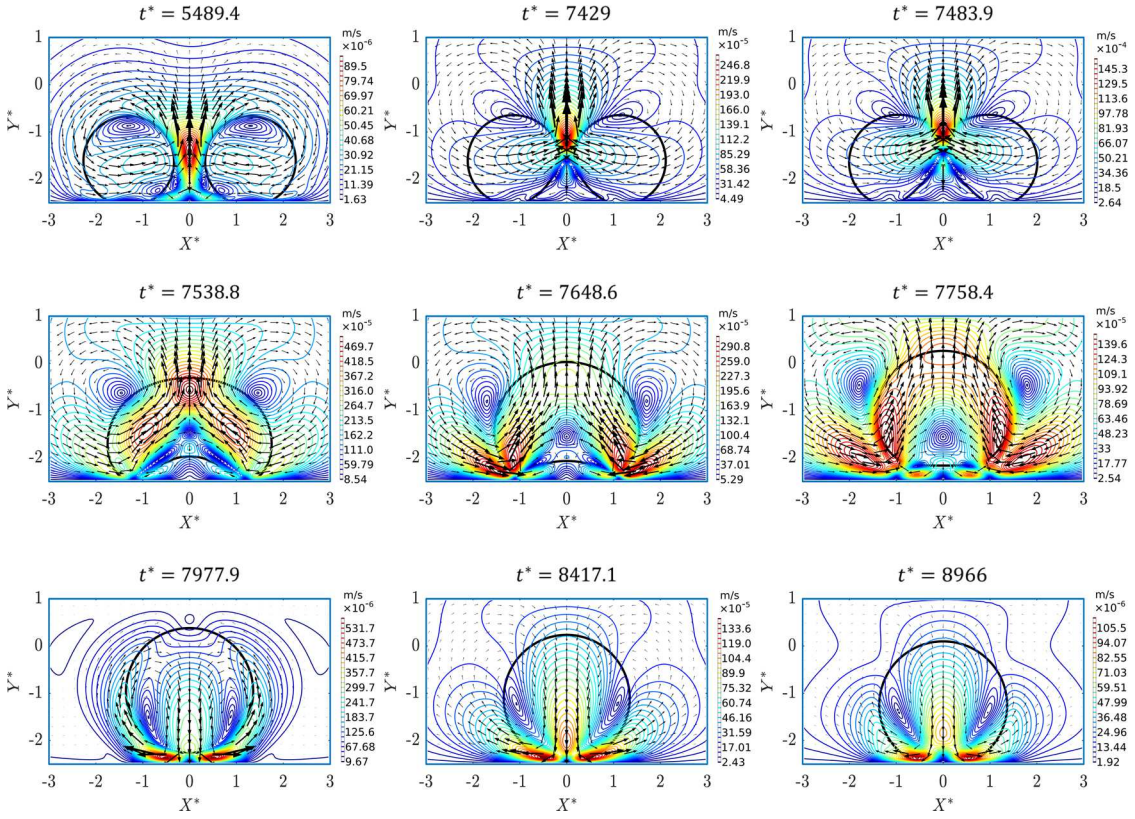

Figure 5. Time evolution of velocity contours both inside and outside of sessile droplets on a hydrophobic surface under a permanent magnetic field at $Bo_m = 0.145$, $\theta_c = 150°$, $\zeta = 1$, and $\lambda = 1$.

contrast, the adhesive force is the main reason behind the adhesion force, where the molecules of the droplet interact with the molecules of the bottom substrate, thereby generating a resistive force that provides resistance against the droplet motion along the substrate. Under the presence of a magnetic field, the magnetic force $\mathbf{F}_m$ dominates over $\mathbf{F}_c$ and $\mathbf{F}_{ad}$, which eventually results in the horizontal movement of the droplets along the direction of the magnet, leading to coalescence between droplets at $Bo_m = 0.145$.

Moreover, during the merging process, the surface energy of the droplets converts into kinetic energy, which in turn aids the merged droplet in jumping upward in the vertical direction from the hydrophobic surface ($t^* = 7648.6$), followed by a gradual decline in the base diameter of the merged droplet ($t^* = 7538.8$). Eventually, as the droplet takes off from the hydrophobic surface, the kinetic energy of the droplet dissipates into the surrounding viscous fluid medium, and the droplet reaches a maximum point where the velocity diminishes to zero ($t^* = 7977.9$). Consequently, as the intensity of kinetic energy diminishes, the magnetic force becomes dominant and drags the droplet back toward the bottom surface of the domain. Finally, the droplet reaches an equilibrium stage where the droplet shape, in addition to the wetted wall condition, is defined by the magnetic and surface tension forces ($t^* = 8966$). The force balance during the droplet jumping phenomenon in the vertical direction (i.e., y axis) can be approximated in the following form

$$\mathbf{F}_k = \mathbf{F}_m + \mathbf{F}_g + \mathbf{F}_d \tag{21}$$

However, when the characteristic dimension of droplets decreases from the macroscopic to the micrometer scale, the effects of gravity become negligible compared to the surface tension and viscous forces, which ultimately govern the droplet dynamics. In general, the gravitational effect can be ignored for droplets that have diameter smaller than the capillary length. In our case, the capillary length is estimated to be 1.04 mm, which is approximately 26 times larger than the droplet size (micrometer size). As a result, the contribution of the gravitational force $\mathbf{F}_g$ (i.e., standard gravity) can be ignored compared to the magnetic force $\mathbf{F}_m$, which ultimately reduces eq 21 in the following format

$$\mathbf{F}_k \approx \mathbf{F}_m + \mathbf{F}_d \tag{22}$$

where $\mathbf{F}_d$ denotes the drag force experienced by the droplet during the upward motion in the opposite direction.

Additionally, the overall trajectory of the droplets in Figure 4b indicates that during the initial stage of the sliding motion, the droplets experience a decline in the apex height and then approach each other along the horizontal direction. Next, as the droplet interfaces come in close contact with each other, the droplets experience an increase in the apex height, which ultimately leads to an upward shift of the droplet positions during the merging stage of droplets. Afterward, following the merging phenomenon, the merged droplet continues to move upward until the kinetic energy of the droplet diminishes to zero through viscous dissipation and then reaches the steady shape under the attractive forces of the magnetic field. Note that a MATLAB code is developed to track the centroids of droplets during the motion, which eventually defines the trajectory of the droplets in Figure 4b,c. Moreover, the trajectory of the merged droplet is illustrated in Figure 4c, which shows that the merged droplet takes a considerable amount of time in reaching the maximum peak during ascension in the vertical direction, while descension leading to a steady-state droplet position is comparatively faster under the influence of the magnetic field.

https://doi.org/10.1021/acs.langmuir.1c00141
Langmuir 2021, 37, 5823−5837

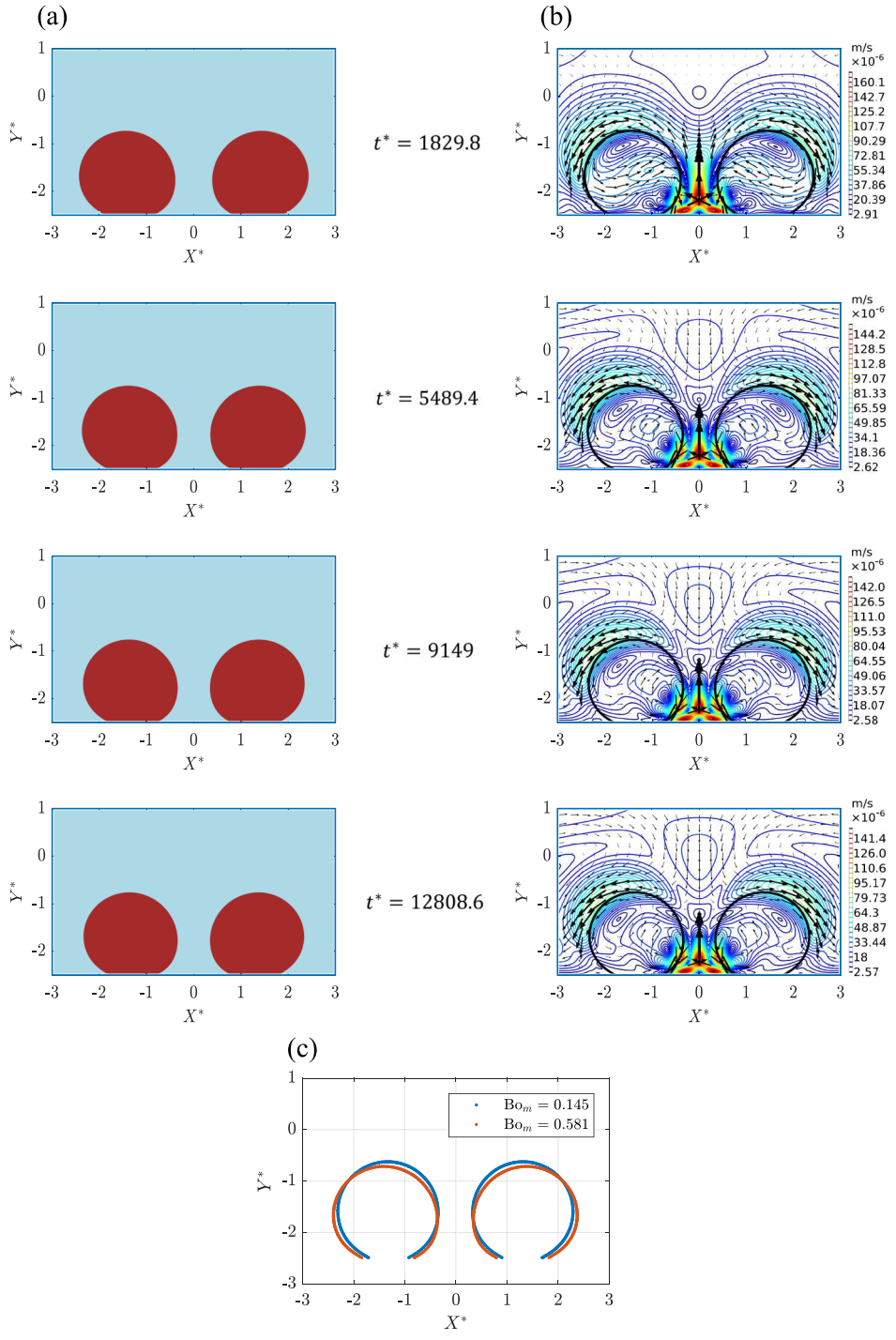

Figure 6. Time evolution of sessile droplets on a hydrophobic surface under a permanent magnetic field at $Bo_m = 0.581$, $\theta_c = 150°$, $\zeta = 1$, and $\lambda = 1$. (a) Droplet shapes; (b) velocity contours; and (c) shapes of droplets during sliding motion under magnetic fields at $t^* = 5489.4$.

Furthermore, the complex flow dynamics behind the interaction between a pair of sessile ferrofluid droplets under a permanent magnetic field can be better explained by the velocity contours around the droplets, and Figure 5 depicts the time evolution of velocity contours both inside and outside of sessile droplets on a hydrophobic surface under a permanent magnetic field at $Bo_m = 0.145$, $\theta_c = 150°$, $\zeta = 1$, and $\lambda = 1$. It can be seen that as the magnetic field is activated, a flow field is created along the horizontal direction, which in turn starts to push the droplets toward the magnet, and as they approach each other, the fluid region between the droplets is squeezed, which gives rise to a larger velocity gradient ($t^* = 5489.4$). Also, during the sliding motion, counter-rotating vortices appear in the bottom and top region of the droplet, where the size of the vortices near the top surface is much larger compared to the vortices near the bottom interface. Consequently, the droplets come into close contact with each other and coalesce into one, which is further followed by a rapid surge in the velocity of the fluid region trapped between the droplets just before merging ($t^* = 7429$). Because the surface energy of the droplets converts into kinetic energy during merging, a larger velocity gradient appears around the merged droplet, where the vortices near the bottom interface

https://doi.org/10.1021/acs.langmuir.1c00141
Langmuir 2021, 37, 5823−5837

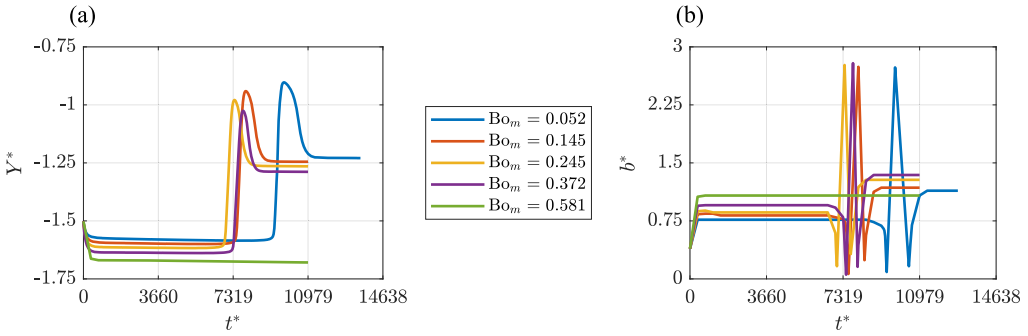

Figure 7. Dynamic behavior of sessile droplets under variable magnetic field strengths at $\theta_c = 150°$, $\zeta = 1$, and $\lambda = 1$. (a) Vertical trajectory Y^* vs t^*; and (b) base diameter b^* vs t^* (the maximum peak represents the diameter of the merged droplet during the jumping phenomenon).

consistently attempt to adhere the droplet to the hydrophobic surface, but eventually fail due to the presence of stronger vortices near the top interface that aid the droplet in taking off from the hydrophobic surface ($t^* = 7538.8$). Eventually, the droplet reaches a maximum peak during jumping, followed by the dissipation of droplet kinetic energy in the surrounding viscous medium ($t^* = 7977.9$) and comes back rapidly on the horizontal surface under the influence of the magnetic field and reaches an equilibrium shape under the prescribed wetted wall condition ($t^* = 8966$). Note that, during the coalescence phenomenon, a drainage of the fluid film between the droplets occurs, which is ultimately followed by the flattening of the interfaces in the merging region. Upon coalescence, a large amount of interfacial energy is released near the merging point, which can be considered as a potential reason behind the increase in the size of the vortices near the top surface compared to the bottom surface at $Bo_m = 0.145$, $\theta_c = 150°$, $\zeta = 1$, and $\lambda = 1$.

Next, we expose the droplets to a comparatively larger magnetic field strength ($Bo_m = 0.581$) to observe how it affects the overall dynamics of a pair of sessile ferrofluid droplets on a hydrophobic surface under similar wetted wall conditions, and Figure 6 represents the time evolution of sessile droplets on the same surface under a permanent magnetic field at $Bo_m = 0.581$, $\theta_c = 150°$, $\zeta = 1$, and $\lambda = 1$. Figure 6a indicates that the droplets undergo greater deformation under stronger magnetic fields (a clear deformation comparison is shown in Figure 6c), which in turn forces the droplet interfaces closer to the magnet to move toward the magnet even more, while experiencing resistance from the interfaces far away from the magnet ($t^* = 1829.8$). Eventually, as time goes on, the droplets spread more under the action of the magnetic field, giving an increase to the magnitude of the base diameter of the droplets ($t^* = 5489.4$). Consequently, the adhesion energy of the droplets due to their larger spread becomes more intense compared to the magnetic force experienced by the droplets ($t^* = 9149$). As a result, the droplets ultimately reach a steady state without undergoing coalescence at $t^* = 12{,}808.6$.

Moreover, the flow-field profiles around the droplets in Figure 6b suggest that during the motion of droplets toward the magnet, a high-pressure region is formed between the droplets near the hydrophobic surface due to the squeezing of the region in between droplets ($t^* = 1829.8$), while a high-pressure region appeared near the top surface of the droplets under comparatively smaller magnetic field strengths at $t^* = 5489.4$ in Figure 5. Also, a significant number of smaller vortices are found to appear near the bottom interface of the droplets, which eventually aid in the movement along the horizontal direction, whereas the larger vortices near the top interface of the droplets tend to resist the motion of droplets, which again emerges due to the movement of the deformed droplets toward the magnet in the horizontal direction ($t^* = 9149$). Finally, under the combined interaction of the magnetic field and droplet adhesion, the droplets reach equilibrium positions on the hydrophobic surface at $t^* = 12{,}808.6$.

Lastly, the dynamic behavior of sessile droplets under variable magnetic field strengths at $\theta_c = 150°$, $\zeta = 1$, and $\lambda = 1$ is summarized in Figure 7. From Figure 7a, it can be seen that as the magnetic field strength increases upto $Bo_m = 0.372$, the droplets experience faster coalescence and the maximum peak reached by the merged droplet decreases. This decrease in the maximum peak can be explained by the fact that due to the increase in the magnetic Bond number, the magnetic force encountered by the merged droplet increases, which in turn provides more resistance during the upward jump from the surface (i.e., maximum peak decreases). Also, as the magnetic field strength starts increasing beyond $Bo_m > 0.245$, the droplets still coalesce and undergo a jumping phenomenon; however, a slight increase in coalescence time is observed compared to the previous lower magnetic Bond number (i.e., $Bo_m = 0.245$). This phenomenon emerges because as the droplets are exposed to much stronger magnetic fields, the spreading of the droplet under the action of the magnetic field increases (Figure 7b), which ultimately increases the adhesion energy of the droplets. As a result, the magnetic field requires a longer time to bring the droplets into closer contact that eventually initiates coalescence and jumping phenomenon off the surface. Moreover, if a significantly stronger magnetic field (i.e., $Bo_m = 0.581$) is applied to the droplets, the droplets experience no coalescence at all and reach steady-state shapes under the combined effect of the magnetic field and wetted wall conditions. Additionally, the effect of magnetic field strength on the spreading diameter of the droplets is depicted in Figure 7b, which clearly shows an increase in the base diameter of the droplets at higher magnetic Bond numbers before and after the coalescence process.

Figure 7a provides very interesting and useful information on the conditions required to induce coalescence/no coalescence between sessile droplets during sliding motion under magnetic fields. Also, during the analysis of this critical condition, unity density and viscosity ratios are used in order to eliminate additional complexities, so that the readers have an easy understanding about the coalescence dynamics of droplets. Here, a dimensionless number (magnetic Bond number Bo_m) is used to relate the contribution of magnetic and surface tension forces, the magnitude of which again can be manually controlled through a change in the magnitude of either initial droplet radius and magnetic field strength or surface tension values. As a result,

https://doi.org/10.1021/acs.langmuir.1c00141
Langmuir 2021, 37, 5823−5837

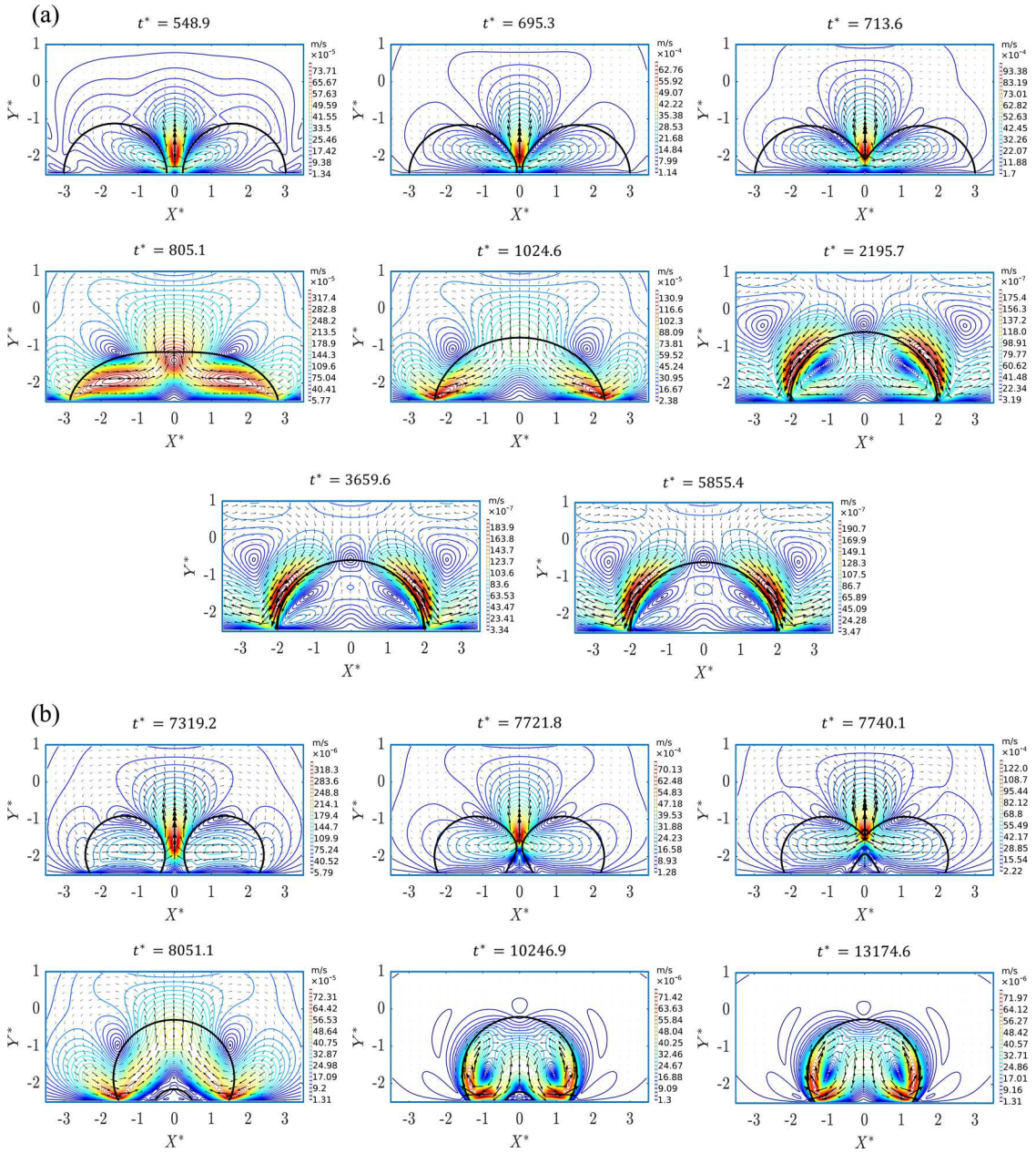

Figure 8. Time evolution of velocity contours around and inside of sessile droplets on a hydrophobic surface under the permanent magnetic field at $Bo_m = 0.145$, $\zeta = 1$, and $\lambda = 1$. (a) $\theta_c = 90°$ and (b) $\theta_c = 120°$.

this analysis can be very beneficial to the experimental design because it clearly provides the magnitudes of all the parameters required to replicate these phenomena during experiments under unity density and viscosity ratios at $\theta_c = 150°$.

Effect of Contact Angles. Now, we investigate the effect of contact angles on the interaction phenomenon between a pair of sessile ferrofluid droplets under magnetic fields, and Figure 8a depicts the time evolution of spreading dynamics of sessile droplets on a hydrophobic surface under the permanent magnetic field at $Bo_m = 0.145$, $\theta_c = 90°$, $\zeta = 1$, and $\lambda = 1$. The shapes of droplets suggest that as they are exposed to a permanent magnetic field at $\theta_c = 90°$, the wettability of the droplets increases and the existence of nonuniform magnetic field contributes in the generation of an asymmetric droplet shapes with respect to the y axis (i.e., the interface of the droplets closer to the permanent magnet experiences greater deformation than the interface far away from the magnet) at $t^* = 548.9$. Moreover, during the spreading process, the interface of the droplets comes closer to each other at $t^* = 695.3$, where a sharp flattening of the interfaces closer to the bottom wall occurs, which eventually initiates the coalescence phenomenon at $t^* = 713.6$. It is important to note that upon initiation of contact, the surface tension force drives a swift motion perpendicular to the line of centers that combines the droplets and causes a decrease in the total surface area ($t^* = 713.6$). Also, as the surface tension force drives the merging process, two large vortices appear on the sides of droplets, while a smaller-sized vortex emerges near the center of the top interface of the merged droplet ($t^* = 805.1$). Subsequently, with the evolution of time, the two large vortices are pushed toward the bottom, while the vortex on the top interface disappears at $t^* = 1024.6$. Finally, the droplet reaches an equilibrium shape at $t^* = 5855.4$.

https://doi.org/10.1021/acs.langmuir.1c00141
Langmuir 2021, 37, 5823−5837

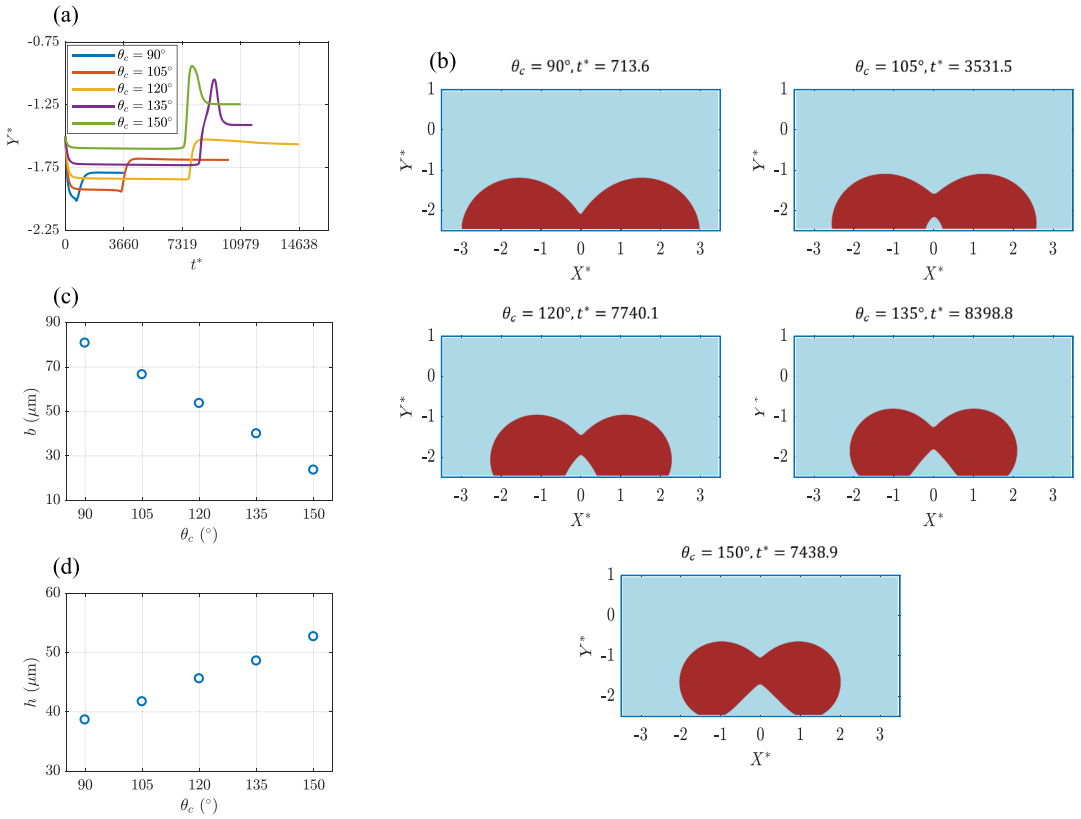

Figure 9. Contact angle effect on the coalescence phenomenon between a pair of hydrophobic droplets under the permanent magnetic field at Bo_m = 0.145, ζ = 1, and λ = 1. (a) Vertical trajectory of droplets; (b) droplet shapes during merging; (c) steady-state droplet base diameter; and (d) steady-state droplet height.

Next, the wetted wall condition of the droplets is changed from θ_c = 90° to θ_c = 120° under the same magnetic field strength, and Figure 8b represents the time evolution of velocity contours around the sessile droplets under a permanent magnetic field at Bo_m = 0.145, θ_c = 120°, ζ = 1, and λ = 1. Compared to the previous case, here, under similar magnetic field strength, the base diameter of the droplets decreases (t^* = 7319.2) and the magnetic field forces the droplet interface closer to the magnet to approach each other (t^* = 7721.8), which begins the coalescence process at t^* = 7740.1. However, because the coalescence process starts around the center of the droplet interfaces, a void appears in the middle near the bottom interface (t^* = 8051.1) during merging, and the droplet tends to take off from the solid surface, which eventually fails due to the dominant nature of magnetic attraction forces and presence of high-pressure regions near the bottom interface of the droplet. Lastly, the droplet settles down and assumes a steady-state shape at t^* = 13,174.6. Note that the merged droplet also takes significantly longer time in reaching a steady-state shape at θ_c = 120° than at θ_c = 90°.

Furthermore, the trajectory of the droplets in Figure 9a indicates that as the contact angle increases upto θ_c = 120°, the merged droplet do not experience any jumping phenomenon, but experiences an increase in its height at the steady state, followed by a decline in height during the approach stage. Also, the time required to initiate coalescence increases with the increase in contact angle values. This phenomenon can be explained by the fact that as the solid surface becomes more hydrophobic, the wettability of the droplet decreases under the same magnetic field strength, which in turn requires more time for the droplets to come into closer contact under the action of the magnetic field. However, as the solid surface starts to become superhydrophobic ($\theta_c \geq 135°$), the kinetic energy of the droplets after the coalescence overcomes the adhesive energy and the droplet ultimately jumps off the surface. Moreover, the merged droplet experiences higher jumping in the vertical direction, as the hydrophobicity of the bottom surface increases, which is attributed by the decrease in the adhesive energy of the droplets (i.e., reduction in base diameter) during the coalescence process (Figure 9b).

The coalescence point between two droplets is a complex phenomenon and strongly dependent on the wettability of the surface (i.e., contact angle) and magnetic field strengths. Figure 9b demonstrates the droplet shapes during merging at Bo_m = 0.145, and the shapes suggest that at θ_c = 90°, the coalescence point occurs near the bottom interface of the droplets, whereas at 105°, the droplets coalesce approximately near the middle of the droplet interfaces. However, as the hydrophobicity of the bottom substrate increases (i.e., $\theta_c \geq$ 120°), the coalescence point appears near the middle of the top half of the droplet interfaces. Nevertheless, the droplet shapes indicate an interesting shift of the coalescence point between droplets from the bottom interface toward the top interface with an increase in the hydrophobicity of the bottom substrate under magnetic fields. Finally, the steady-state characteristics of the merged droplet are illustrated in Figure 9c,d, which shows a decrease and an increase in the base diameter and the height of the droplet, respectively, under increasing contact angle values.

Effect of Viscosity Ratios. In the final section, we focus on analyzing the effect of viscosity ratios on the coalescence phenomenon between a pair of hydrophobic sessile droplets under the permanent magnetic field at Bo_m = 0.145, θ_c = 150°,

https://doi.org/10.1021/acs.langmuir.1c00141
Langmuir 2021, 37, 5823−5837

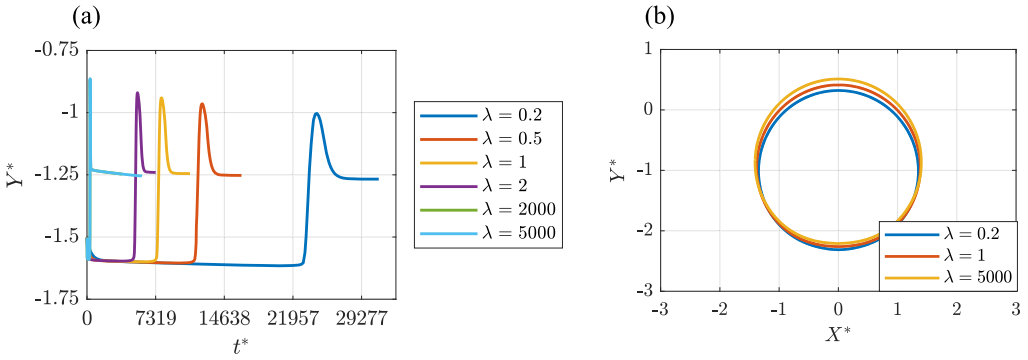

Figure 10. Viscosity ratio effect on the coalescence phenomenon between a pair of hydrophobic sessile droplets under the permanent magnetic field at $Bo_m = 0.145$, $\theta_c = 150°$, and $\zeta = 1$. (a) Vertical trajectory of droplets and (b) droplet shapes at maximum peaks.

and $\zeta = 1$. Here, the viscosity of the droplets is kept constant, while the viscosity of the continuous phase is varied to observe how the behavior of sessile droplets change in different surrounding media under the nonuniform magnetic field, including air where the properties of air medium give rise to huge contrast in viscosity ratios (i.e., $\lambda \approx 5000$).

From Figure 10a it can be seen that irrespective of viscosity ratios, the droplets, followed by a sliding motion toward the magnet, coalesce and experience the jumping phenomenon under the exposure to a permanent magnetic field; however, the maximum peak reached by the merged droplet during jumping increases with the increase in viscosity ratios. This happens because as the viscosity of the surrounding medium decreases, the kinetic energy of the droplets after merging requires longer time to get dissipated into the surroundings, that is, the droplet undergoes higher jumping in the vertical direction. Also, in addition to a decline in the coalescence time with the increase in viscosity ratios, the merged droplet requires comparatively smaller time to return to the solid surface and reach a steady state under a magnetic field. Interestingly, the trajectory of droplets at a viscosity ratio beyond 2000 (i.e., $\lambda \geq 2000$) is found to overlap with each other, which also indicates the dominant behavior of the magnetic field at higher viscosity ratios. Furthermore, the droplet shapes at maximum peaks for some representative viscosity ratios are depicted in Figure 10b, which demonstrates a small increase in the droplet jumping in the vertical direction compared to the massive change in viscosity ratios.

In the research community, 2D studies are extremely popular compared to three-dimensional (3D) studies for providing flexibilities in terms of investigating the effects of a wide range of parameters on droplet dynamics, while saving a considerable amount of computational resources. Also, before moving on to the in-detailed investigation of the droplet dynamics under magnetic fields, the 2D model is systematically validated against benchmark solutions and existing experimental works in the literature to make sure that it is capable of capturing the correct droplet interface and producing accurate results. Although a 3D model would be more realistic than a 2D model, it would generate a similar coalescence phenomenon under similar conditions; however, the droplet shapes could be slightly different due to the effect of surface tension in the z-direction.

CONCLUSIONS

A systematic numerical inquiry on the dynamics between a pair of sessile droplets on a smooth hydrophobic surface under a permanent magnetic field is carried out in this paper. The results indicate that a nonuniform magnetic field is capable of increasing the wettability of a hydrophobic surface, which usually has lower surface energy and interfacial tension between the droplet and solid surface. Consequently, the base diameter of the sessile droplet experiences an increase at higher magnetic field strengths, while the apex height and equilibrium contact angle decreases. Also, when a pair of sessile droplets are symmetrically separated with respect to the center of the magnet along y-axis on a superhydrophobic surface (i.e., $\theta_c = 150°$), the merged droplet experiences a jumping phenomenon off the solid surface, which is eventually followed by the migration of the droplets along the horizontal direction that ultimately leads to coalescence under the action of the nonuniform magnetic field. Moreover, as the magnetic field strength increases upto $Bo_m = 0.372$, the droplets still experience coalescence at a faster rate; however, the maximum peak reached by the merged droplet during the upward flight decreases. Furthermore, if the magnetic field strength is allowed to increase above $Bo_m > 0.372$, at $Bo_m = 0.581$, the droplets do not encounter any coalescence phenomenon anymore, instead reach equilibrium shapes under the combined effects of the magnetic field and wetted wall conditions.

Additionally, we investigated the effect of contact angles on the dynamic interaction behavior between a pair of sessile droplets under magnetic fields, and the findings suggest the existence of a critical contact angle value, below which the droplets do not experience any jumping off phenomenon after undergoing coalescence. In our investigation, the critical contact angle value is found to be approximately 120° (i.e., $\theta_c^{cr} \approx 120°$). Also, the merging pattern of droplets changes at lower contact angle values (i.e., $\theta_c = 90°$). Moreover, the merged droplet sustains an attenuation in equilibrium base diameter magnitudes, while experiencing an increase in the apex height on more hydrophobic surfaces. Furthermore, on a superhydrophobic surface (i.e., $\theta_c = 150°$), as the viscosity ratio increases (i.e., $\lambda = 5000$ in case of air as the surrounding medium), the droplets encounter rapid coalescence under the attraction forces of the magnetic field, and the merged droplet experiences higher jumping at higher magnitudes of viscosity ratios. Nevertheless, the findings signify the massive potential of the magnetic field in the controlled transportation of sessile droplets on a hydrophobic surface that will be critical to a significant number of biological and chemical assays.

https://doi.org/10.1021/acs.langmuir.1c00141
Langmuir 2021, 37, 5823−5837

■ ASSOCIATED CONTENT

Supporting Information

The Supporting Information is available free of charge at https://pubs.acs.org/doi/10.1021/acs.langmuir.1c00141.

Mass conservation of the droplet and grid independence check (PDF)

■ AUTHOR INFORMATION

Corresponding Author

Cheng Wang − *Department of Mechanical and Aerospace Engineering, Missouri University of Science and Technology, Rolla, Missouri 65409, United States;* orcid.org/0000-0001-7630-4906; Email: wancheng@mst.edu

Authors

Md Rifat Hassan − *Department of Mechanical and Aerospace Engineering, Missouri University of Science and Technology, Rolla, Missouri 65409, United States*

Jie Zhang − *Department of Mechanical and Aerospace Engineering, Missouri University of Science and Technology, Rolla, Missouri 65409, United States*

Complete contact information is available at: https://pubs.acs.org/10.1021/acs.langmuir.1c00141

Notes

The authors declare no competing financial interest.

■ ACKNOWLEDGMENTS

The authors gratefully acknowledge the support from the Department of Mechanical and Aerospace Engineering (MAE) and the Center for Biomedical Research (CBR) at Missouri University of Science and Technology. This work is partially supported by the NSF through grant DMS-1818642 to C.W.

■ REFERENCES

(1) Keng, P. Y.; Chen, S.; Ding, H.; Sadeghi, S.; Shah, G. J.; Dooraghi, A.; Phelps, M. E.; Satyamurthy, N.; Chatziioannou, A. F.; Kim, C.-J. C.; et al. Micro-chemical synthesis of molecular probes on an electronic microfluidic device. *Proc. Natl. Acad. Sci. U.S.A.* **2012**, *109*, 690−695.

(2) Javed, M. R.; Chen, S.; Lei, J.; Collins, J.; Sergeev, M.; Kim, H.-K.; Kim, C.-J.; van Dam, R. M.; Keng, P. Y. High yield and high specific activity synthesis of [18 F] fallypride in a batch microfluidic reactor for micro-PET imaging. *Chem. Commun.* **2014**, *50*, 1192−1194.

(3) Ng, A. H.; Chamberlain, M. D.; Situ, H.; Lee, V.; Wheeler, A. R. Digital microfluidic immunocytochemistry in single cells. *Nat. Commun.* **2015**, *6*, 7513.

(4) Pipper, J.; Zhang, Y.; Neuzil, P.; Hsieh, T.-M. Clockwork PCR including sample preparation. *Angew. Chem.* **2008**, *120*, 3964−3968.

(5) Pipper, J.; Inoue, M.; Ng, L. F.-P.; Neuzil, P.; Zhang, Y.; Novak, L. Catching bird flu in a droplet. *Nat. Med.* **2007**, *13*, 1259−1263.

(6) Choi, K.; Ng, A. H. C.; Fobel, R.; Chang-Yen, D. A.; Yarnell, L. E.; Pearson, E. L.; Oleksak, C. M.; Fischer, A. T.; Luoma, R. P.; Robinson, J. M.; et al. Automated digital microfluidic platform for magnetic-particle-based immunoassays with optimization by design of experiments. *Anal. Chem.* **2013**, *85*, 9638−9646.

(7) Choi, K.; Ng, A. H. C.; Fobel, R.; Wheeler, A. R. Digital microfluidics. *Annu. Rev. Anal. Chem.* **2012**, *5*, 413−440.

(8) Nelson, W. C.; Kim, C.-J. C. Droplet actuation by electrowetting-on-dielectric (EWOD): A review. *J. Adhes. Sci. Technol.* **2012**, *26*, 1747−1771.

(9) Fair, R. B. Digital microfluidics: is a true lab-on-a-chip possible? *Microfluid. Nanofluid.* **2007**, *3*, 245−281.

(10) Cho, S. K.; Moon, H.; Kim, C.-J. Creating, transporting, cutting, and merging liquid droplets by electrowetting-based actuation for digital microfluidic circuits. *J. Microelectromech. Syst.* **2003**, *12*, 70−80.

(11) Chiou, C.-H.; Shin, D. J.; Zhang, Y.; Wang, T.-H. Topography-assisted electromagnetic platform for blood-to-PCR in a droplet. *Biosens. Bioelectron.* **2013**, *50*, 91−99.

(12) Zhang, Y.; Shin, D. J.; Wang, T.-H. Serial dilution via surface energy trap-assisted magnetic droplet manipulation. *Lab Chip* **2013**, *13*, 4827−4831.

(13) Zhang, Y.; Wang, T.-H. Full-range magnetic manipulation of droplets via surface energy traps enables complex bioassays. *Adv. Mater.* **2013**, *25*, 2903−2908.

(14) Lehmann, U.; Vandevyver, C.; Parashar, V. K.; Gijs, M. A. M. Droplet-based DNA purification in a magnetic lab-on-a-chip. *Angew. Chem., Int. Ed.* **2006**, *45*, 3062−3067.

(15) Ding, X.; Li, P.; Lin, S.-C. S.; Stratton, Z. S.; Nama, N.; Guo, F.; Slotcavage, D.; Mao, X.; Shi, J.; Costanzo, F.; et al. Surface acoustic wave microfluidics. *Lab Chip* **2013**, *13*, 3626−3649.

(16) Wang, Z.; Zhe, J. Recent advances in particle and droplet manipulation for lab-on-a-chip devices based on surface acoustic waves. *Lab Chip* **2011**, *11*, 1280−1285.

(17) Zhang, Y.; Nguyen, N.-T. Magnetic digital microfluidics−a review. *Lab Chip* **2017**, *17*, 994−1008.

(18) Long, Z.; Shetty, A. M.; Solomon, M. J.; Larson, R. G. Fundamentals of magnet-actuated droplet manipulation on an open hydrophobic surface. *Lab Chip* **2009**, *9*, 1567−1575.

(19) Mats, L.; Young, R.; Gibson, G. T. T.; Oleschuk, R. D. Magnetic droplet actuation on natural (Colocasia leaf) and fluorinated silica nanoparticle superhydrophobic surfaces. *Sens. Actuators, B* **2015**, *220*, 5−12.

(20) Kim, J. A.; Kim, M.; Kang, S. M.; Lim, K. T.; Kim, T. S.; Kang, J. Y. Magnetic bead droplet immunoassay of oligomer amyloid β for the diagnosis of Alzheimer' s disease using micro-pillars to enhance the stability of the oil−water interface. *Biosens. Bioelectron.* **2015**, *67*, 724−732.

(21) Shikida, M.; Takayanagi, K.; Inouchi, K.; Honda, H.; Sato, K. Using wettability and interfacial tension to handle droplets of magnetic beads in a micro-chemical-analysis system. *Sens. Actuators, B* **2006**, *113*, 563−569.

(22) Park, M. C.; Kim, M.; Lim, G. T.; Kang, S. M.; An, S. S. A.; Kim, T. S.; Kang, J. Y. Droplet-based magnetic bead immunoassay using microchannel-connected multiwell plates (μCHAMPs) for the detection of amyloid beta oligomers. *Lab Chip* **2016**, *16*, 2245−2253.

(23) Okochi, M.; Tsuchiya, H.; Kumazawa, F.; Shikida, M.; Honda, H. Droplet-based gene expression analysis using a device with magnetic force-based-droplet-handling system. *J. Biosci. Bioeng.* **2010**, *109*, 193−197.

(24) Shi, X.; Chen, C.-H.; Gao, W.; Chao, S.-h.; Meldrum, D. R. Parallel RNA extraction using magnetic beads and a droplet array. *Lab Chip* **2015**, *15*, 1059−1065.

(25) Lehmann, U.; Hadjidj, S.; Parashar, V. K.; Vandevyver, C.; Rida, A.; Gijs, M. A. M. Two-dimensional magnetic manipulation of microdroplets on a chip as a platform for bioanalytical applications. *Sens. Actuators, B* **2006**, *117*, 457−463.

(26) Beyzavi, A.; Nguyen, N.-T. One-dimensional actuation of a ferrofluid droplet by planar microcoils. *J. Phys. D: Appl. Phys.* **2008**, *42*, 015004.

(27) Beyzavi, A.; Nguyen, N.-T. Modeling and optimization of planar microcoils. *J. Micromech. Microeng.* **2008**, *18*, 095018.

(28) Rida, A.; Fernandez, V.; Gijs, M. A. M. Long-range transport of magnetic microbeads using simple planar coils placed in a uniform magnetostatic field. *Appl. Phys. Lett.* **2003**, *83*, 2396−2398.

(29) Hassan, M. R.; Zhang, J.; Wang, C. Deformation of a ferrofluid droplet in simple shear flows under uniform magnetic fields. *Phys. Fluids* **2018**, *30*, 092002.

(30) Zhang, J.; Hassan, M. R.; Rallabandi, B.; Wang, C. Migration of ferrofluid droplets in shear flow under a uniform magnetic field. *Soft Matter* **2019**, *15*, 2439−2446.

(31) Hassan, M. R.; Wang, C. Magnetic field induced ferrofluid droplet breakup in a simple shear flow at a low Reynolds number. *Phys. Fluids* **2019**, *31*, 127104.
(32) Hassan, M. R.; Wang, C. Ferro-hydrodynamic interactions between ferrofluid droplet pairs in simple shear flows. *Colloids Surf., A* **2020**, *602*, 124906.
(33) Hassan, M. R.; Wang, C. Lateral migration of a ferrofluid droplet in a plane Poiseuille flow under uniform magnetic fields. *Phys. Rev. E* **2020**, *102*, 022611.
(34) Hassan, M. R.; Zhang, J.; Wang, C. Numerical investigation of falling ferrofluid droplets under magnetic fields. *Colloid Interface Sci. Commun.* **2021**, *40*, 100333.
(35) Bitar, A.; Kaewsaneha, C.; Eissa, M. M.; Jamshaid, T.; Tangboriboonrat, P.; Polpanich, D.; Elaissari, A. Ferrofluids: from preparation to biomedical applications. *J. Colloid Sci. Biotechnol.* **2014**, *3*, 3−18.
(36) Raj, K.; Moskowitz, R. Commercial applications of ferrofluids. *J. Magn. Magn. Mater.* **1990**, *85*, 233−245.
(37) Reena Mary, A. P.; Narayanan, T.; Sunny, V.; Sakthikumar, D.; Yoshida, Y.; Joy, P.; Anantharaman, M. Synthesis of bio-compatible spion−based aqueous ferrofluids and evaluation of radiofrequency power loss for magnetic hyperthermia. *Nanoscale Res. Lett.* **2010**, *5*, 1706−1711.
(38) Nguyen, N.-T.; Zhu, G.; Chua, Y.-C.; Phan, V.-N.; Tan, S.-H. Magnetowetting and sliding motion of a sessile ferrofluid droplet in the presence of a permanent magnet. *Langmuir* **2010**, *26*, 12553−12559.
(39) Beyzavi, A.; Nguyen, N.-T. Programmable two-dimensional actuation of ferrofluid droplet using planar microcoils. *J. Micromech. Microeng.* **2009**, *20*, 015018.
(40) Egatz-Gómez, A.; Melle, S.; García, A. A.; Lindsay, S. A.; Márquez, M.; Domínguez-García, P.; Rubio, M. A.; Picraux, S. T.; Taraci, J. L.; Clement, T.; et al. Discrete magnetic microfluidics. *Appl. Phys. Lett.* **2006**, *89*, 034106.
(41) Kovetz, A.; Olund, B. The effect of coalescence and condensation on rain formation in a cloud of finite vertical extent. *J. Atmos. Sci.* **1969**, *26*, 1060−1065.
(42) Menchaca-Rocha, A.; Martínez-Dávalos, A.; Nunez, R.; Popinet, S.; Zaleski, S. Coalescence of liquid drops by surface tension. *Phys. Rev. E: Stat., Nonlinear, Soft Matter Phys.* **2001**, *63*, 046309.
(43) Bellehumeur, C. T.; Bisaria, M. K.; Vlachopoulos, J. An experimental study and model assessment of polymer sintering. *Polym. Eng. Sci.* **1996**, *36*, 2198−2207.
(44) Madejski, J. Solidification of droplets on a cold surface. *Int. J. Heat Mass Transfer* **1976**, *19*, 1009−1013.
(45) Ashgriz, N. *Handbook of Atomization and Sprays: Theory and Applications*; Springer Science & Business Media, 2011.
(46) Geng, H.; Feng, J.; Stabryla, L. M.; Cho, S. K. Dielectrowetting manipulation for digital microfluidics: Creating, transporting, splitting, and merging of droplets. *Lab Chip* **2017**, *17*, 1060−1068.
(47) Bithi, S. S.; Wang, W. S.; Sun, M.; Blawzdziewicz, J.; Vanapalli, S. A. Coalescing drops in microfluidic parking networks: A multifunctional platform for drop-based microfluidics. *Biomicrofluidics* **2014**, *8*, 034118.
(48) Guo, M. T.; Rotem, A.; Heyman, J. A.; Weitz, D. A. Droplet microfluidics for high-throughput biological assays. *Lab Chip* **2012**, *12*, 2146−2155.
(49) Liu, F.; Ghigliotti, G.; Feng, J. J.; Chen, C.-H. Numerical simulations of self-propelled jumping upon drop coalescence on non-wetting surfaces. *J. Fluid Mech.* **2014**, *752*, 39−65.
(50) Cheng, Y.; Xu, J.; Sui, Y. Numerical investigation of coalescence-induced droplet jumping on superhydrophobic surfaces for efficient dropwise condensation heat transfer. *Int. J. Heat Mass Transfer* **2016**, *95*, 506−516.
(51) Nam, Y.; Kim, H.; Shin, S. Energy and hydrodynamic analyses of coalescence-induced jumping droplets. *Appl. Phys. Lett.* **2013**, *103*, 161601.
(52) Shi, Y.; Tang, G. H.; Xia, H. H. Investigation of coalescence-induced droplet jumping on superhydrophobic surfaces and liquid condensate adhesion on slit and plain fins. *Int. J. Heat Mass Transfer* **2015**, *88*, 445−455.
(53) Liu, X.; Cheng, P.; Quan, X. Lattice Boltzmann simulations for self-propelled jumping of droplets after coalescence on a super-hydrophobic surface. *Int. J. Heat Mass Transfer* **2014**, *73*, 195−200.
(54) Wang, X.; Chen, Z.; Xu, B. Coalescence-induced jumping of condensate droplets on microstructured surfaces with different gravitational fields by lattice Boltzmann method. *Comput. Fluids* **2019**, *188*, 60−69.
(55) Liu, J.; Liu, S. Dynamics behaviors of droplet on hydrophobic surfaces driven by electric field. *Micromachines* **2019**, *10*, 778.
(56) Du, G.-S.; Pan, J.-Z.; Zhao, S.-P.; Zhu, Y.; den Toonder, J. M. J.; Fang, Q. Cell-based drug combination screening with a microfluidic droplet array system. *Anal. Chem.* **2013**, *85*, 6740−6747.
(57) Ma, Y.; Pan, J.-Z.; Zhao, S.-P.; Lou, Q.; Zhu, Y.; Fang, Q. Microdroplet chain array for cell migration assays. *Lab Chip* **2016**, *16*, 4658−4665.
(58) Zhu, Y.; Zhang, Y.-X.; Cai, L.-F.; Fang, Q. Sequential operation droplet array: an automated microfluidic platform for picoliter-scale liquid handling, analysis, and screening. *Anal. Chem.* **2013**, *85*, 6723−6731.
(59) Garcia-Cordero, J. L.; Fan, Z. H. Sessile droplets for chemical and biological assays. *Lab Chip* **2017**, *17*, 2150−2166.
(60) Ueda, E.; Geyer, F. L.; Nedashkivska, V.; Levkin, P. A. DropletMicroarray: facile formation of arrays of microdroplets and hydrogel micropads for cell screening applications. *Lab Chip* **2012**, *12*, 5218−5224.
(61) Zhu, Y.; Zhang, Y.-X.; Liu, W.-W.; Ma, Y.; Fang, Q.; Yao, B. Printing 2-dimentional droplet array for single-cell reverse transcription quantitative PCR assay with a microfluidic robot. *Sci. Rep.* **2015**, *5*, 9551.
(62) Berthier, J. *Micro-drops and Digital Microfluidics*; William Andrew, 2012.
(63) COMSOL, CFD Module Application Library Manual.
(64) Rosensweig, R. E. *Ferrohydrodynamics*; Courier Corporation, 2013.

https://doi.org/10.1021/acs.langmuir.1c00141
Langmuir 2021, 37, 5823−5837